Journal of Catalysis 280 (2011) 150–160

Contents lists available at ScienceDirect

Journal of Catalysis

journal homepage: www.elsevier.com/locate/jcat

0.5 wt.% Pd/C catalyst for purification of terephthalic acid: Irreversible deactivation in industrial plants

R. Pellegrini [a,*], G. Agostini [b], E. Groppo [b], A. Piovano [b], G. Leofanti [a,c], C. Lamberti [b]

[a] Chimet SpA—Catalyst Division, Via di Pescaiola 74, I-52041 Viciomaggio (Arezzo), Italy
[b] Department of Inorganic, Physical and Materials Chemistry, INSTM Reference Center and NIS Centre of Excellence, Università di Torino, Via P. Giuria 7, I-10125 Torino, Italy
[c] Consultant, Via Firenze 43, 20010 Canegrate (Milano), Italy

ARTICLE INFO

Article history:
Received 18 October 2010
Revised 10 March 2011
Accepted 17 March 2011
Available online 29 April 2011

Keywords:
Supported Pd catalyst
Terephthalic acid
Catalyst deactivation
Sintering
Poisoning
Pd_4S
Pd_3Pb
XRPD
TEM
EDS

ABSTRACT

A systematic study on several spent catalysts, withdrawn from different terephthalic acid purification reactors loaded with the same fresh catalyst (0.5 wt.% Pd/C, type D3065, supplied by Chimet SpA), has been carried out. Spent catalysts characterized by different lifetimes, position in the catalytic bed, sintering degree, and types of contaminant (mainly S, Pb, and Mo) have been investigated by TEM coupled with EDS detection, XRPD, EXAFS spectroscopy, and CO chemisorption. The Pd sintering process involves all catalysts, irrespective of the nature and amount of contaminants that have no influence on sintering rate except for S poisoning. Pd sintering occurs following different steps, leading to the formation of larger crystals, aggregates, and agglomerates, the last being the primary cause of the loss of Pd surface area and, consequently, of the decrease in catalytic activity. Among the investigated contaminants, S and Pb are the worst, because they strongly interact with Pd, forming from surface adlayers (not detectable by XRPD, but visible by EDS mapping) up to bulk Pd_4S or Pd_3Pb alloys (easily detectable by XRPD). In both cases, the catalytic activity decreases. In contrast, Mo, Cr, Fe, Ti, and Al do not interact preferentially with Pd (no alloys have been detected, although the contaminants are present in relevant concentrations): They have been found to be spread on the whole catalyst surface. Accordingly, no direct effect of these contaminants on catalytic activity loss has been evidenced.

1. Introduction

Terephthalic acid (TA) is an important intermediate used for the manufacture of polyethylene terephthalate (PET), which is mainly applied in the production of fibers and bottles [1]. In the Amoco MC process, TA production starts from the homogeneous phase oxidation of *p*-xylene in acetic acid solvent, using Co, Mn, and Br as constituents of the catalytic system [2]:

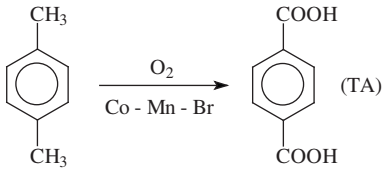

The crude terephthalic acid (CTA) so obtained contains around 3000 ppm of 4-carboxybenzaldehyde (4-CBA) as well as colored polyaromatic compounds (yellow compounds) [2,3]. Being a monofunctional compound, the 4-CBA lowers the polymerization rate and the average molecular weight of the polymer; on the other hand, colored impurities confer a polymer color that is undesired for fiber manufacture [4,5]. Therefore, CTA is purified by hydrogenation in water at 270–290 °C over a granular 0.5 wt.% Pd/C catalyst. In this way, the 4-CBA is converted into *p*-toluic acid that is more soluble than 4-CBA and thus remains in the mother liquid after crystallization; at the same time, the yellow compounds are hydrogenated to colorless compounds [4]:

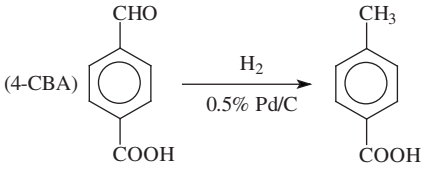

PTA is a fast-growing material: Worldwide production went from 24 million tons in 2000 [6] to about 42 million tons in 2006 [7]. The worldwide consumption of granular 0.5 wt.% Pd/C used for the final purification step well exceeds the 1000 tons per year. This catalyst is composed of nanodispersed palladium particles

* Corresponding author. Fax: +39 0575 441424.
E-mail address: riccardo.pellegrini@chimet.com (R. Pellegrini).

0021-9517/$ - see front matter © 2011 Elsevier Inc. All rights reserved.
doi:10.1016/j.jcat.2011.03.012

supported on 4 × 8 mesh size coconut activated carbon and is packed in a column-type reactor. The catalyst life differs from plant to plant, as many deactivation phenomena can contribute to the decay of catalyst performance. The main cause of catalyst deactivation is palladium sintering, but some other phenomena may also take place, such as palladium loss, poisoning, and deposition of metallic terephthalates or polymers [8]. A thorough characterization of exhausted catalysts can give important feedback to both catalyst manufacturers and catalyst end users, so that the former can improve the catalyst design (e.g., to have better resistance to sintering), while the latter can improve the catalyst use and avoid unexpected catalyst deactivation in order to prolong the catalyst life.

With the aim of expanding upon previous knowledge on the causes of catalyst deactivation [8], we have characterized several spent catalysts withdrawn from different catalytic industrial reactors, exhibiting different lifetimes and types of contaminant (mainly S, Pb, and Mo). In all the PTA production plants considered in this study, the original fresh catalyst was supplied by Chimet SpA (0.5 wt.% Pd/C type D3065) and this allows significant comparison among different spent catalysts. As the packed catalytic bed is crossed by the CTA solution from top to bottom, whenever possible the spent catalyst has been withdrawn from different levels inside the reactor (hereafter indicated as top, middle, and bottom) in order to get information on the distribution of contaminants and the sintering profile along the entire catalytic bed.

Palladium sintering and contamination with S, Pb, Mo, Cr, Fe, Ti, and Al have been studied by TEM coupled with EDS detection, XRPD, EXAFS, and CO chemisorption. Possible deactivation by deposition of polymeric materials has not been investigated, because, in contrast to irreversible sintering and poisoning, the catalyst may be regenerated by washing with NaOH solution. In any case, no encapsulation of Pd particles has been detected in the samples studied in the present work. Structural, compositional, and morphological characterizations of spent catalysts have been coupled with measurement of residual catalytic activity.

2. Experimental

2.1. Catalysts

The list of investigated samples, their lifetimes in industrial reactors, and concentrations of main contaminants are given in Table 1. The first entry (F) is the fresh catalyst (0.5 wt.% Pd/C, type D3065, supplied by Chimet SpA), while the second (A) is obtained from the fresh catalyst after an aging treatment carried out in an autoclave in the presence of hydrogen and water at 277 °C for 24 h. The latter sample simulates the rapid stabilization occurring during the first working hours of the catalyst inside an industrial reactor. All the other samples are spent catalysts, named by S followed by a number indicating the different plants or runs. The labels TOP, MID, and BOT refer to the position inside the catalytic bed (top, middle, and bottom, respectively).

The samples have been divided into several groups: (i) sintering has been investigated on F, A, and S1 samples, (ii) S contamination on S2 samples, (iii) Pb contamination on S3–S5 samples, (iv) simultaneous S and Pb contamination on S6 samples, and (v) Mo contamination on S7 samples. Finally, the effects of other, less important contaminants, such as Cr, Fe, Ti, and Al, have been analyzed by selecting proper samples from series S6–S7.

To study the S poisoning mechanism, S-poisoned catalysts have been prepared starting from the fresh catalyst (F), which has been exposed to different aging treatments in an autoclave at 277 °C for 24 h with hydrogen and an aqueous solution containing either Na_2SO_4 (S/Pd = 10 at/at) or Na_2S (S/Pd = 5 at/at).

2.2. Characterization

2.2.1. Elemental analysis

Metal contamination has been determined by ICP. Catalyst samples were previously calcined at 550 °C, and the ashes so obtained were exposed to acidic attack.

Table 1
List of investigated samples: F = fresh, A = aged in laboratory, S = spent from industrial plant.

Code	Lifetime (month)	Main contaminants (ppm)	Pd		Pd_4S		Pd_3Pb		Relative activity
			⟨D⟩ (Å)	(%)	⟨D⟩ (Å)	(%)	⟨D⟩ (Å)	(%)	
F	–	None	136[a]	100	–	–	–	–	–
A	–	None	139[a]	100	–	–	–	–	1.00
S1	27	Cr(330) Mo(142)	244	100	–	–	–	–	0.11
S2-TOP	6	S(low)[b] Mo(400) Cr(106)	233	64	240	36	–	–	0.10
S2-MID	6	S(medium)[b] Mo(220) Cr(83)	340	39	368	61	–	–	0.10
S2-BOT	6	S(high)[b] Mo(262) Cr(150) Ti(105)	337	22	427	78	–	–	0.12
S3-TOP	9	Pb(680) Mo(380) Cr(130) Al(225)	178	46	–	–	198	54	0.07
S3-BOT	9	Pb(550) Mo(250) Cr(85) Al(250)	151	52	–	–	157	48	0.11
S4-TOP	14	Pb(1350) Mo(890) Cr(1120) Fe(95) Ti(410)	204	31	–	–	178	69	0.05
S5-TOP	14	Pb(1600) Mo(1020) Cr(1620) Fe(112) Ti(445)	235	37	–	–	212	63	0.05
S6-TOP	1.5	S(low)[b] Pb(320) Mo(115)	165	100	–	–	–	–	0.06
S6-MID	1.5	S(low)[b] Pb(110) Mo(73)	151	100	–	–	–	–	0.12
S6-BOT	1.5	S(low)[b] Pb(28) Mo(55)	181	100	–	–	–	–	0.11
S7-TOP	15	Mo(2000)	224	100	–	–	–	–	0.15
S7-MID	15	Mo(1400)	217	100	–	–	–	–	0.16
S7-BOT	15	Mo(310)	251	100	–	–	–	–	0.15

Note: The number following the S code indicates the different plants or runs. Suffix TOP, MID, and BOT refer to the region of the reactor where the spent catalyst was extracted: top, middle, and bottom, respectively. Number of working months inside the reactor and main contaminants are also reported. The relative fraction of Pd metal and, when present, of Pd_4S or Pd_3Pb alloys with respect to the total crystalline phases (as determined by Rietveld refinement) is also reported, together with the average crystal size, estimated by applying the Scherrer equation to the Pd(1 1 1), Pd_4S(2 1 0), and Pd_3Pb(1 1 1) reflections. The last column refers to the residual catalytic activity, normalized to the activity of the catalyst stabilized in the laboratory (sample A).

[a] For samples F and A, only a fraction of Pd contributes to the Bragg diffraction and the data reported in the table represent the average crystal size of this fraction. For these samples, the mean particle size, obtained from CO chemisorption (according to the geometrical model described elsewhere [18]), is 41 and 84 Å for F and A, respectively.

[b] A quantitative determination of sulfur poisoning is not possible because of the interference of 200–400 ppm of sulfur unavoidably present in the coconut activated carbon.

2.2.2. X-ray powder diffraction (XRPD)

X-ray powder diffraction patterns were collected with a PW3050/60 X'Pert PRO MPD diffractometer from PANalytical working in the Debye–Scherrer geometry, using as a source the high-powered ceramic tube PW3373/10 LFF with a Cu anode equipped with a Ni filter to attenuate K_β and focused by a PW3152/63 X-ray mirror. Scattered photons have been collected by an RTMS (real time multiple strip) X'celerator detector. Powdered samples have been hosted inside a 0.8-mm boron silicate capillary and mounted on a rotating goniometer head.

The average crystal diameter $\langle D\rangle$ has been obtained by applying the Scherrer equation, $\langle D\rangle = K\lambda/\beta\cos(\theta_{\mathrm{Bragg}})$, where λ is the wavelength of the Cu Kα radiation (1.541 Å), K the shape factor (fixed to 0.9 according to the literature regarding Pd nanoparticles [9]), and β is the 2θ FWHM (corrected by the instrumental broadening) of the Pd(1 1 1), Pd_4S(2 1 0), and Pd_3Pb(1 1 1) reflections. Although the absolute $\langle D\rangle$ values can be affected by systematic errors, the size trend observed on different samples is reliable. When a second crystalline phase has been observed (Pd_4S or Pd_3Pb), the relative fraction of metal and alloy with respect to the total crystalline phases contributing to the Bragg scattering has been estimated with a Rietveld approach [10,11], using the TOPAS code [12]. These data are summarized in Table 1.

2.2.3. Extended X-ray absorption fine structure (EXAFS) spectroscopy

X-ray absorption experiments at the Pd *K*-edge (24350 eV) were performed at the BM26A beamline [13,14] of the ESRF facility (Grenoble, F). The white beam has been monochromatized using a Si(1 1 1) double crystal; harmonic rejection has been performed using Pt-coated silicon mirrors. The following experimental geometry has been adopted: (1) I_0 (10% efficiency); (2) sample; (3) I_1 (40% efficiency); (4) reference Pd foil; (5) I_2 (80% efficiency). This setup allows direct energy/angle calibration for each spectrum, avoiding any problem related to small energy shifts due to small thermal instability of the monochromator crystals [15]. The EXAFS part of the spectra has been collected with a variable sampling step in energy, resulting in $\Delta k = 0.05$ Å^{-1}, up to 20 Å^{-1}, with an integration time that increases linearly with k from 4 to 25 s/point to account for the low signal-to-noise ratio at high k values.

The extraction of the $\chi(k)$ function has been performed using the Athena code [16]. For each sample, two consecutive EXAFS spectra have been collected and corresponding $\chi(k)$ functions were averaged before data analysis. EXAFS data analysis was performed using the Arthemis software [16]. Phase and amplitudes have been calculated by FEFF6 code [17] and successfully checked with Pd metal foil. For each sample, the averaged $k^3\chi(k)$ function has been Fourier transformed in the $\Delta k = 2.00$–15.75 Å^{-1} interval.

2.2.4. Transmission electron microscopy (TEM) coupled with energy dispersive spectroscopy (EDS)

TEM analysis has been performed by means of a JEOL 3010-UHR HRTEM microscope operating at 300 kV, equipped with a ($2k \times 2k$)-pixel Gatan US1000 CCD camera and with an OXFORD INCA EDS instrument for atomic recognition via energy dispersive spectroscopy (EDS). Due to the large size of the catalyst grains (4×8 mesh), catalyst samples have been gently ground by hand to make the thickness of the carbon grains compatible with TEM measurements and then deposited on a copper grid covered with a lacey carbon film.

2.2.5. CO chemisorption

Chemisorption has been performed by the dynamic pulse method on a Micromeritics Autochem 2910 instrument using CO as a probe molecule at 50 °C. Catalyst samples have been dried at 120 °C overnight and prereduced in situ with H_2 at 120 °C. As explained elsewhere [18], a CO/Pd average stoichiometry of 1 has been assumed for calculation of the dispersion. This technique has been applied to fresh (F) and stabilized (A) samples only. In fact, CO chemisorption on exhausted catalysts could be misleading because of the presence of metal contaminants potentially able to adsorb CO and/or because of the partial surface covering of the active Pd phase by polymers or other contaminants.

2.3. Catalytic activity

Catalytic activity has been measured in a batch reactor under working conditions strictly similar to the industrial ones. A mixture of 4-CBA in PTA (3000 ppm) has been hydrogenated in a 20% water solution at 277 °C and 5 bar hydrogen partial pressure. Analysis of the reaction mixture has been carried out by HPLC. Activity data have been expressed as a rate constant derived from the first-order plot of 4-CBA concentration vs. time. Values reported in Table 1 have been normalized with respect to the activity of the catalyst stabilized in the laboratory (sample A).

3. Results and discussion

3.1. Palladium sintering

Inside the industrial hydropurification reactor working at 270–290 °C, the catalyst undergoes a sintering of Pd particles, which is an unavoidable cause of catalyst deactivation over several months [19]. This phenomenon is caused by both high Pd mobility on the carbon surface and high local Pd concentrations. Concerning the first point, Pd mobility is favored by the weak Pd–carbon interaction [20]. Coming to the second point, the nominal Pd loading on granular carbon is as low as 0.5 wt.%. However, as previously demonstrated [8], Pd is located preferentially in the external layer of carbon granules (eggshell distribution), where it reaches a local concentration as high as 10–20 wt.%. The sum of the two factors (high Pd mobility and concentration) causes a progressive sintering even when the catalyst works under correct conditions.

Based on our experience, the industrial performance of a Pd catalyst operating under proper conditions typically undergoes rapid (several hours to a few days) stabilization, followed by smooth decay over several months. Therefore, to investigate the whole sintering process over the catalyst life, three samples have been analyzed as follows: (i) the fresh catalyst (F); (ii) the catalyst aged in the laboratory (A), which simulates the rapid stabilization occurring in the industrial reactor; and (iii) the spent catalyst that has worked inside an industrial reactor under correct conditions for 27 months (S1), which contains only a small amount of contaminants (Table 1). These three samples have been characterized by XRPD, CO chemisorption, and TEM. It is worth noting that each of the aforementioned techniques is able to sample different fractions of the Pd atoms; therefore, careful coupling of the results obtained by the three independent techniques is mandatory to avoid misleading interpretations. As an example, both XRPD and TEM techniques provide information only on a fraction of the total Pd particles, whereas CO chemisorption, although sensitive to the whole Pd surface, is not informative on the homogeneity of the Pd phase.

The 35–90° angular range of XRPD patterns of the three samples (inset of Fig. 1) is dominated by the scattering of the carbon support broad reflections centered around $2\theta = 43°$ and 80°. To better appreciate the contribution of the supported phases, the background due to the carbon support has been subtracted from the original patterns, and reported in the region $35° < 2\theta < 50°$, where the most intense Pd peaks are present (main part of Fig. 1). All of the XRPD patterns are characterized by a series of reflections at 2θ values of 40.1°, 46.7°, 68.2°, and 82.2°, corresponding to the

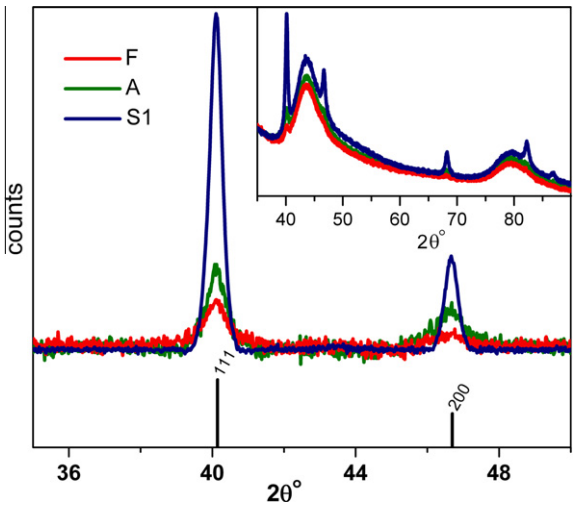

Fig. 1. XRPD patterns of F, A, and S1 samples, as collected (inset) and after subtraction of the carbon background (main part). Vertical lines show the indexed Pd reflections.

(1 1 1), (2 0 0), (2 2 0), and (3 1 1) planes of the Pd metal phase [21].

The intensity of the diffraction peaks and their FWHM β give information on the Pd fraction responsible for scattering and on the average size of the corresponding Pd crystals, respectively.

Moving from the fresh (F) to the stabilized (A) catalyst, the intensity of the Pd fcc peaks increases, whereas β remains nearly constant. The observation provides evidence that the fraction of Pd detectable by XRPD is larger in sample A than in sample F, but the corresponding average crystal size does not change. In this stage, the sintering involves only the smaller Pd crystals, which grow to a size similar to the size of larger crystals of fresh catalyst. These latter do not appear to be significantly involved in the sintering. Accordingly, CO chemisorption data indicate that the fraction of available surface atoms in sample A decreases by a factor of 2 with respect to sample F: The CO/Pd ratio goes from 0.256 to 0.125, which roughly corresponds to the doubling of the mean Pd crystal size, from 41 to 84 Å.

The XRPD pattern of the spent catalyst (S1) shows a large increase in the intensity of the diffraction peaks, accompanied by a decrease in β. However, although the fraction of Pd giving Bragg diffraction increases by more than one order of magnitude, the average size of the Pd crystalline domains increases only by 75–80%.

To better understand the sintering process, the three samples have been investigated by TEM. Selected micrographs of samples F, A, and S1 are reported in Fig. 2a and b, c and d, and e and f, respectively. Generally speaking, TEM investigation makes it possible to obtain [18,22,23] the following: (i) qualitative information on the presence of aggregates of particles; (ii) quantitative information on shape and size distribution of isolated particles. Conversely, the determination of $\langle D \rangle$ for single individual particles belonging to an aggregate is not possible, because the absence of contrast precludes a clear definition of particle borders.

In catalyst F, the fraction of aggregated particles is small (see circled regions in Fig. 2a). Well-defined cubo-octahedral particles are observed (Fig. 2b), characterized by an asymmetric particle size distribution, having an average diameter of 23 Å and a standard deviation of 6 Å. This $\langle D \rangle$ value is significantly smaller than that obtained by CO chemisorption (41 Å, see Table 1), because the aggregates cannot be included in the TEM statistics.

In sample A (Fig. 2c and d), there are much fewer isolated nanoparticles and the majority of Pd is in the form of aggregated ensembles. Therefore, a quantitative evaluation of the particle size distribution cannot be made. Qualitatively, we observe an increase in the average particle size, in agreement with CO chemisorption data. Finally, TEM images of sample S1 do not show any more well-defined and isolated cubo-octahedral particles, but only large particles (Fig. 2f) or, mainly, aggregates (Fig. 2e) with a size in the range 200–500 Å.

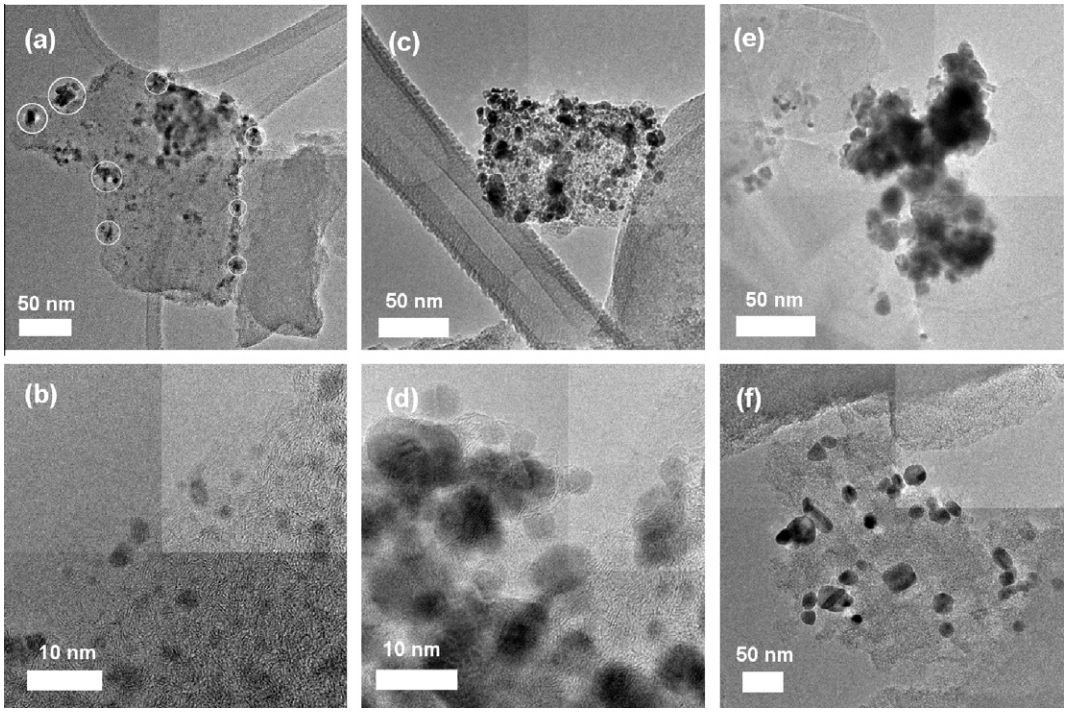

Fig. 2. Selected TEM micrographs representing samples F, A, and S1, parts (a and b), (c and d), and (e and f), respectively. For samples F and A, the top and bottom parts are at low and high magnification, respectively. The aggregation of Pd in sample S1 is so high that only low-magnification images are meaningful.

The TEM images discussed above clarify the evolution of both intensity and average Pd crystal size obtained from the diffraction peaks of the XRPD patterns shown in Fig. 1. By comparing the data obtained with the three independent techniques, the following conclusions can be reached: (i) in sample F, the large majority of Pd particles are isolated (TEM) and have dimensions smaller than 30 Å, and so do not contribute to the XRPD pattern. A minor fraction is made up of larger particles, mainly belonging to aggregates, detectable by XRPD with a mean size of 136 Å. The overall mean size of the Pd particles (CO chemisorption) is 41 Å. (ii) Sample A contains both small particles observed by TEM (Fig. 2d), still below the detection limit of XRPD, and an increased fraction of larger particles, as individual or aggregated, having dimension up to 200–300 Å (Fig. 2c), which contribute to the XRPD pattern. Due to the sintering process, the mean size of Pd particles detected by CO chemisorption is increased to 84 Å. (iii) In sample S1, nearly all the Pd particles are sufficiently sintered to be detectable by XRPD and, consequently, the average crystal size of 244 Å, determined using the Scherrer equation, is representative of the whole Pd population. On these bases, we can conclude that during the early working hours of the catalyst inside the hydrogenation reactor (stabilization step), the Pd particles progressively increase in crystal size according to a classical sintering phenomenon (growth of small crystals). Simultaneously, isolated Pd particles start to aggregate, although they maintain their own crystalline domain and, therefore, most of their surface area (Fig. 2d). At longer working times (sample S1), the classical sintering is progressively switched off because of the consumption of isolated particles on the few-nm scale (Fig. 2f) and the particle aggregation proceeds (Fig. 2e), ending finally in the formation of agglomerates, where adjacent particles are welded together. This phenomenon becomes the primary cause of the loss of Pd surface area on the long time scale and, consequently, of the decrease in catalytic activity.

The samples discussed up to now have been chosen to investigate the sintering phenomenon because they do not show any relevant poisoning (see Table 1). However, the Pd sintering process involves all catalysts, irrespective of the nature and amount of contaminants. A quantitative evaluation of the growth of Pd crystal size during industrial runs is shown in the main part of Fig. 3 for all the samples reported in Table 1. After a fast increase during the initial period, slow and almost linear growth of crystal size as a function of lifetime is observed irrespective of the type and concentration of contaminant. Some S-poisoned samples of S2 series (6-month data) are an exception, as will be discussed in the next section. The crystal size of mixed phases (such as Pd_4S and Pd_3Pb) arising from contamination, as detected by XRPD, is close to the size of the fraction of noncontaminated Pd crystals in the same sample. This is visualized in the inset of Fig. 3 which shows that the crystal size of contaminated compounds (Pd_4S or Pd_3Pb) changes linearly with that of uncontaminated Pd particles on the same sample. As far as the second sintering mechanism is concerned (agglomeration and welding of individual particles), qualitative observations by TEM have not shown any significant differences in $\langle D \rangle$ between noncontaminated and contaminated regions (discriminated by EDS mapping). In addition, all the investigated spent catalysts contain agglomerates of particles, partially welded together, as previously discussed for sample S1. We can thus conclude that sintering of Pd particles is driven mainly by temperature and time, with the exception of crystal growth in S-poisoned catalysts.

Finally, in spite of the presence of a small temperature gradient along the reactor, sintering is substantially independent of the sample position inside the reactor (Fig. 3).

Notice that the catalysts investigated in this study have been selected to be representative of the different deactivation phenomena encountered in industrial plants. Consequently, the main part of Fig. 3 does not represent the real population of spent catalysts. In fact, the large majority of spent catalysts are deactivated by sintering after more than 15 months of life inside industrial reactors and so would be comparable only to catalyst S1, whose service life is 27 months.

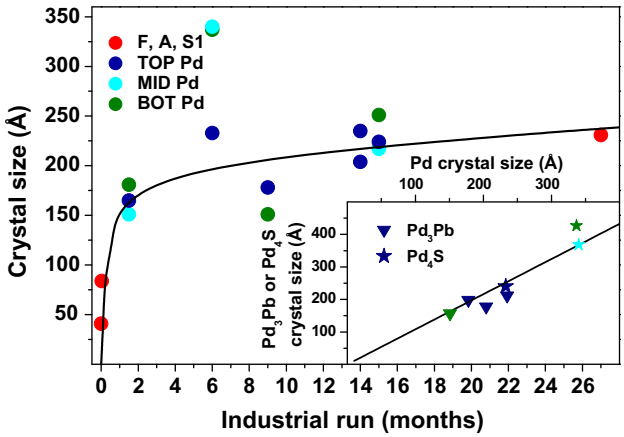

Fig. 3. Main part: average crystal size, as determined by the Scherrer equation, of the whole set of investigated samples as a function of the catalyst lifetime inside industrial reactors. Pd particle sizes of samples F and A have been calculated from dispersion measured by CO chemisorption assuming cubo-octahedral Pd particles with 5/6 exposed surface because the fraction of Pd crystals giving rise to Bragg diffraction is not representative of the whole Pd population. Inset: average crystal size of contaminated Pd compounds (Pd_4S, stars, and Pd_3Pb, triangles) determined as for Pd as a function of average Pd crystal size (the color code differentiates the TOP, MID, and BOT parts of the reactor, as in the main part). (For interpretation of the references to color in this figure legend, the reader is referred to the web version of this article.)

3.2. Contamination by S (S2 series)

Sulfur is one of the most common contaminants of Pd catalysts used in PTA production, because S compounds may be present in initial *p*-xylene feedstock, and also in hydrogen gas and process water. It is known that, under reducing conditions, S compounds adsorb dissociatively on metal surfaces, leaving a reduced S atom strongly bonded to the surface [24]. In principle, S adsorption may have a double influence on catalyst performance as follows: (i) reducing the fraction of accessible Pd surface sites and (ii) changing their electronic properties [24]. Moreover, a Pd_4S bulk sulfide [25] has been also found in deactivated Pd catalysts [8].

To investigate all these processes, three catalysts coming from different parts of the same reactor and showing S contamination have been analyzed in detail (S2 series in Table 1). First, TEM measurements combined with EDS analysis have been used to investigate the relative spatial distribution of the different elements. A representative TEM micrograph and the corresponding EDS map are shown in Fig. 4a and b. White and red colors refer to regions where only Pd or only S fluorescence photons have been collected, respectively; cyan color refers to regions where Pd and S are simultaneously present. An analysis carried out on several Pd particles revealed that, when detected, the S signal is always overlapped with that of Pd, but some S-free Pd particles have also been observed. This evidence suggests that, in most cases, Pd and S form a mixed compound.

The structure of the mixed compound and its amount relative to nonpoisoned Pd have been determined by X-ray diffraction. All the XRPD patterns (Fig. 4c) show two series of reflections superimposed on the broad peaks already assigned to the carbon support. The first series of reflections is due to Pd metal, while the second series is characterized by reflections at 2θ equal to 35.2°, 36.6°,

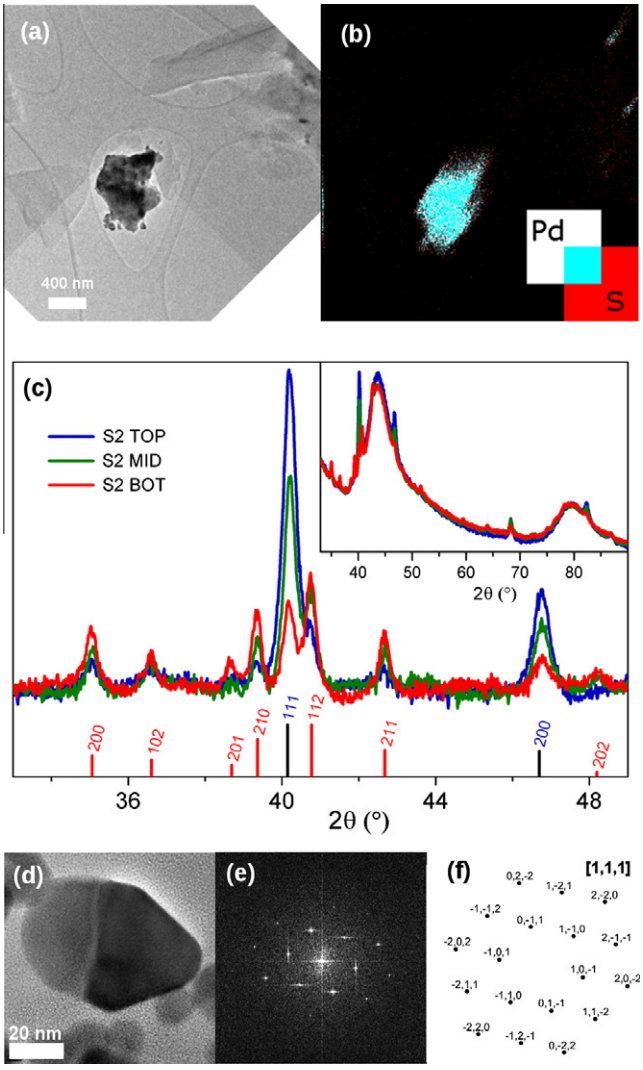

Fig. 4. Analysis of samples poisoned by S. (a) Selected TEM micrograph representing sample S2-BOT. (b) EDS map of the same region shown in part (a), allowing speciation of Pd and S elements to be done. Regions where only Pd or only S fluorescence photons have been collected are evidenced in white and red colors, respectively; cyan color refers to regions where Pd and S are simultaneously present. (c) XRPD patterns of S2-TOP, -MID, -BOT as collected (inset) and after subtraction of the carbon background (main part). Vertical black and red lines show indexed Pd and Pd_4S reflections, respectively. (d) TEM image of a Pd_4S nanoparticle oriented along the [1, 1, 1] zone axis, as determined by its FT (e) and corresponding simulated diffraction pattern (f). (For interpretation of the references to color in this figure legend, the reader is referred to the web version of this article.)

38.8°, 39.5°, 40.8°, 42.8°, 48.2°, 51.6°, 59.6°, 63.9°, and 72.5°, which are ascribable to the (2 0 0), (1 0 2), (2 0 1), (2 1 0), (1 1 2), (2 1 1), (2 0 2), (2 1 2), (3 1 1), (3 0 2), and (1 1 4) planes of the Pd_4S phase [26]. This last assignment is confirmed by electron diffraction performed on a single crystal well oriented with respect to the electron beam (Fig. 4d). The Fourier transform (Fig. 4e) matches the simulated pattern of a Pd_4S crystal oriented along the [1, 1, 1] zone axis (Fig. 4f). Although the Pd_4S phase is present in all three investigated samples of S2 series, its concentration is not uniform along the catalytic bed, but increases from top to bottom. The relative fraction of Pd_4S obtained by a Rietveld analysis increases from 36% (S2-TOP), through 61% (S2-MID), to 78% (S2-BOT), as summarized in Table 1.

XRPD clearly proves the presence of a crystalline Pd_4S phase with an evident gradient along the reactor bed. However, both amorphous and small size ($\langle D \rangle$ below 30 Å) crystalline domains escape XRPD detection. To verify whether the trend observed by XRPD reflects the whole Pd population in the S2 series, the presence of Pd_4S phase has been studied by EXAFS spectroscopy (Fig. 5a and b). As is well known, the Pd metal fcc structure consists of a Pd first shell formed by 12 equivalent Pd atoms located at 2.75 Å [21]. When S enters the Pd lattice, forming the Pd_4S compound (having a tetragonal cell with $a = b = 5.1147$ Å and $c = 5.5903$ Å, space group 114) [26], in the first Pd coordination shell two S atoms substitute for two Pd atoms, at 2.34 and 2.48 Å, respectively. This substitution causes a relevant distortion of the whole first shell structure, so that the remaining 10 Pd–Pd distances are no longer equivalent, but spread over the range 2.76–3.12 Å ($\langle R_{Pd-Pd} \rangle = 2.87$ Å). This R_{Pd-Pd} heterogeneity affects the FT of the EXAFS signals, as demonstrated by the simulated spectra of Pd and Pd_4S phases (Fig. 5c and d). In particular, limiting the discussion to the first shell only, the Pd_4S spectrum is characterized by a lower intensity of the |FT| and by an imaginary part shifted toward greater distances with respect to the spectrum of the metal Pd. On these bases, it is clear that the EXAFS spectra of the S-poisoned samples (Fig. 5a and b) confirm the progressive transformation of Pd into Pd_4S from top to bottom of the catalytic bed, as already evidenced by XRPD analysis. In fact, going from S2-TOP to S2-BOT, a progressive decrease in the first shell intensity (Fig. 5a), a shift of the imaginary part toward greater distances (Fig. 5b), and, finally, a nearly complete disappearance of the higher shell contribution (not shown in the reported R-range) are observed.

The increase in Pd_4S content from top to bottom in the catalytic bed can be explained by taking into account that in the reactor feed (i.e., CTA and water) the S contaminant is present in a high oxidation state (i.e., SO_4^{2-}). In fact, S from any possible source (e.g., in the *p*-xylene feed) is transformed into SO_4^{2-} in the oxidation unit preceding the hydropurification unit. Furthermore, S contamination of process water commonly occurs in the form of SO_4^{2-} rather than S^{2-}. It is known that the toxicity of S increases as the oxidation state diminishes [24]. Therefore, we hypothesize that high temperatures and reducing conditions (such as those characterizing the TA purification) can transform less harmful SO_4^{2-} into poisonous S^{2-}. In this way, the SO_4^{2-} ions entering the reactor from the top should be reduced to the more poisonous S^{2-} ions along the catalytic bed, leading to Pd_4S formation.

To prove that SO_4^{2-} can be converted into poisonous S^{2-} under industrial reaction conditions, the fresh catalyst has been subjected to different aging treatments in the autoclave (see Section 2.1). When the catalyst is treated in an aqueous solution of Na_2SO_4 (S/Pd = 10 at/at) under hydrogen at 277 °C for 24 h, no S^{2-} ions are detected in the mother solution by colorimetric analysis and the catalytic activity is the same as for the catalyst stabilized following the standard procedure (sample A), i.e., in water without Na_2SO_4 (Table 2). On the other hand, when the aging treatment has been performed using an aqueous solution of Na_2S (S/Pd = 5 at/at), the catalytic activity has dropped abruptly (Table 2). A similar decrease in activity has been observed by aging the catalyst in an aqueous solution of Na_2SO_4 (S/Pd = 10 at/at), as done previously, but in the presence of terephthalic acid; in this case, S^{2-} was detected by colorimetric analysis in the mother solution. These results demonstrate that the presence of an acidic environment allows the transformation of SO_4^{2-} into S^{2-} (H_2S). Simultaneously, the catalyst is self-poisoned by formation of Pd_4S, as detected by XRPD (pattern not reported for brevity). The data discussed above explain why the Pd_4S amount increases from top to bottom of the reactor: The SO_4^{2-} ions present in the reactor feed are gradually transformed into S^{2-} (H_2S) along the catalytic bed and so the terephthalic acid solution is progressively enriched with S^{2-}, which acts as a poison and is responsible for the Pd_4S formation.

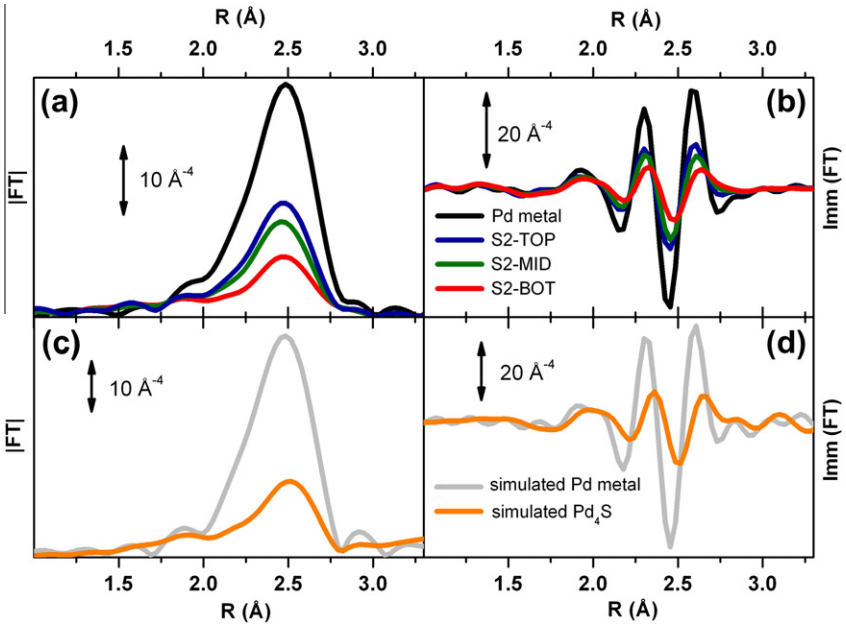

Fig. 5. Modulus (a) and imaginary part (b) of the k^3-weighted, phase-uncorrected FT of the EXAFS spectra of the samples contaminated by S: S2-TOP (blue curve), S2-MID (green curve), and S2-BOT (red curve). For comparison, the spectrum of bulk Pd foil (black line) is also reported. (c) and (d) as (a) and (b) for the simulated spectra, performed by FEFF6, of Pd metal and Pd_4S bulk models (ΔE = 0 eV; $S_0^2 = 1$; σ^2 = 0.005 Å^2). (For interpretation of the references to color in this figure legend, the reader is referred to the web version of this article.)

Table 2
Catalytic activity of fresh catalyst subjected to different aging treatments carried out in the autoclave with hydrogen and water at 277 °C for 24 h.

Contaminant	S/Pd (at/at)	Presence of terephthalic acid	Relative activity
SO_4^{2-} (from Na_2SO_4)	10	No	1.02
S^{2-} (from Na_2S)	5	No	0.04
SO_4^{2-} (from Na_2SO_4)	10	Yes	0.07

Note: The addition of either Na_2SO_4 or Na_2S has been investigated as well as the addition of terephthalic acid (20 wt.%). Catalytic activity has been normalized to the activity of the catalyst stabilized in laboratory (sample A in Table 1).

As far as the Pd and Pd_4S crystal size is concerned, the following remarks can be made: (i) at low Pd_4S concentration (sample S2-TOP), the crystal size of Pd particles lies very close to the sintering curve (blue circle at 6 months in Fig. 3) and (ii) with increasing Pd_4S concentration (samples S2-MID and S2-BOT), the crystal size of Pd lies significantly above the sintering curve (cyan and green circles at 6 months in Fig. 3). In addition, the crystal sizes of both phases, unpoisoned Pd and Pd_4S, on the same sample are comparable (stars in the inset of Fig. 3). Only on sample S2-BOT, the conversion of Pd into Pd_4S is so high that it counteracts the tendency for residual Pd crystals to grow. These results evidence that S poison increases the sintering rate, as suggested by [27]. As will be discussed in Section 3.7, the contamination by S did not happen linearly with time, but S probably contacted the catalyst during the last period of its lifetime, causing rapid decay of catalyst performance.

3.3. Contamination by Pb (S3, S4, and S5 series)

Generally speaking, Pb is considered a poison for metal catalysts [19,28] and in particular for Pd catalysts, where Pb is purposely used to moderate Pd activity in selective hydrogenation reactions [29,30]. In poisoning experiments carried out on Pd catalysts treated with Pb^{2+} and other metal species under mild conditions ($22 \leqslant T \leqslant 77$ °C and 1 bar), Mallat et al. [31] claimed that the poisoning effect consists of coverage of the Pd surface by Pb adatoms and in the diffusion of adsorbed Pb into the bulk Pd. However, evidence of the occurrence of such a mechanism inside an industrial reactor is not available.

Herein, we report data on four catalysts poisoned by Pb coming from three different reactors; this evidences that contamination by Pb is a problem common to many industrial plants. Indeed, Pb is an impurity of the Co- and Mn-based catalyst used in the oxidation of *p*-xylene to terephthalic acid (see Section 1), and this could explain the presence of Pb in the CTA feedstock of the hydrogenation reactor.

A representative TEM micrograph and the corresponding EDS map are shown in Fig. 6a, b. About half of the observed Pd particles do not show Pb contamination but, when present, the signal of Pb strictly correlates with that of Pd (see map), suggesting the formation of a mixed compound.

The presence of a possible mixed phase has been verified by XRPD (Fig. 6c), where samples S3-TOP and S3-BOT show two series of reflections superimposed on the carbon background. The first series of reflections is due to the Pd metal phase, while the second series is characterized by reflections at 2θ equal to 38.6°, 44.9°, 65.4°, 78.6°, and 82.8°, which are ascribable to the (1 1 1), (2 0 0), (2 2 0), (3 1 1), and (2 2 2) planes of the Pd_3Pb phase [32]. Also in this case, this assignment is confirmed by electron diffraction performed on a single crystal well oriented to the electron beam. Fig. 6d reports the TEM image of a Pd_3Pb nanoparticle; the corresponding FT, reported in Fig. 6e, matches the pattern simulated for a Pd_3Pb crystal oriented along the [0, 1, 1] zone axis (Fig. 6f). Besides the reflections characteristic of Pd and Pd_3Pb, the XRPD patterns of samples S4-TOP and S5-TOP show a third series of reflections due to Na_2CO_3 and a single reflection at 2θ = 39.4° due to an unassigned extra phase (evidenced with a star in Fig. 6c).

Na_2CO_3 is a residue of catalyst washing with NaOH, which is a typical treatment for catalyst regeneration [33]. Catalysts S4-TOP and S5-TOP have been washed with NaOH inside the industrial reactor as an attempt to regenerate the catalyst after a sudden decrease in catalytic performance was observed.

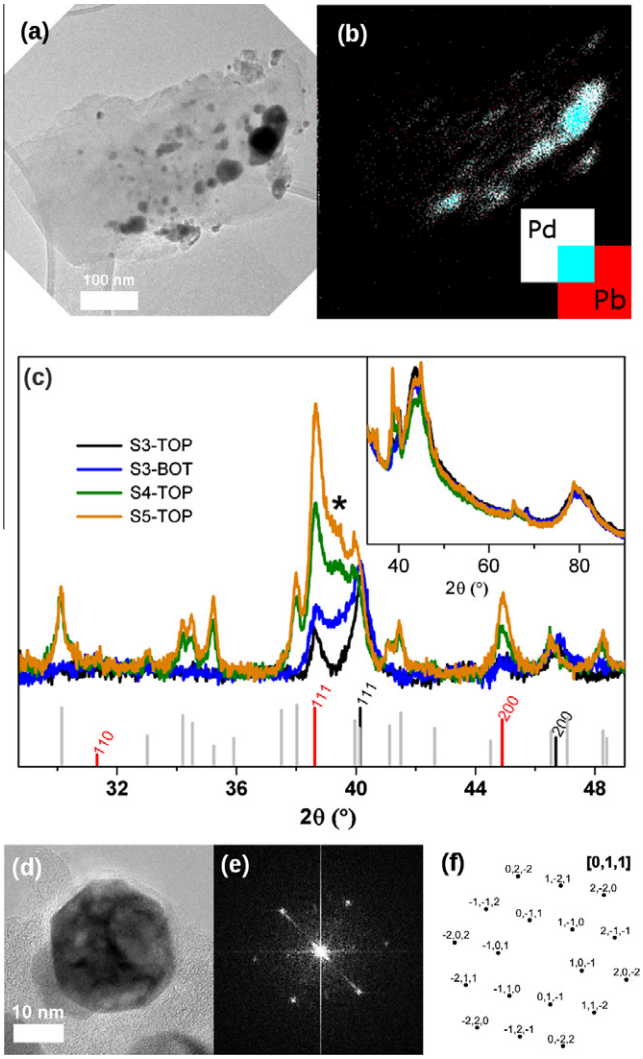

Fig. 6. Analysis of samples poisoned by Pb. (a) Selected TEM micrograph representing sample S5-TOP. (b) EDS map of the same region shown in (a) allowing speciation of Pd and Pb elements to be done. Regions where only Pd or only Pb fluorescence photons have been collected are evidenced in white and red, respectively; cyan refers to regions where Pd and Pb are simultaneously present. (c) XRPD patterns of S3-TOP, S3-BOT, S4-TOP, and S5-TOP, as collected (inset) and after subtraction of the carbon background (main part). Vertical black and red lines show the indexed Pd and Pd_3Pb reflections, respectively. Also reported, although not indexed, are the reflections of Na_2CO_3 phase (gray lines). (d) HRTEM image of a Pd_3Pb nanoparticle oriented along the [0, 1, 1] zone axis, as determined by its FT (e) and corresponding simulated diffraction pattern (f). (For interpretation of the references to color in this figure legend, the reader is referred to the web version of this article.)

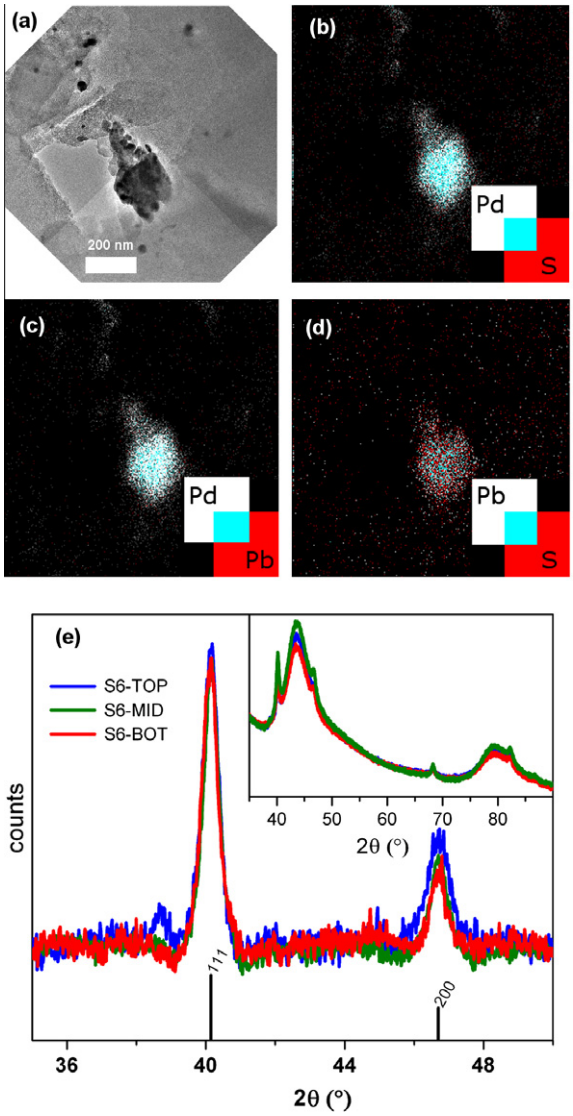

Fig. 7. Analysis of samples simultaneously poisoned by Pb and S. (a) Selected TEM micrograph representing sample S6-TOP. (b–d) EDS maps of the same region shown in (a), showing the correlation between the fluorescence signals of Pd and S, Pd and Pb, and Pb and S, respectively. (e) XRPD patterns of S6-TOP, S6-MID, and S6-BOT.

The fractions of Pd and Pd_3Pb phases, evaluated by Rietveld analysis, are reported in Table 1. Notice that the results obtained for samples S4-TOP and S5-TOP are less accurate than the others, because in the XRPD patterns, reflections characteristic of three different phases (i.e., Pd, Pd_3Pb, and Na_2CO_3) are overlapped and a further unassigned peak in the $37.5° < 2\theta < 40.7°$ region is present. Nevertheless, it is evident that samples S4-TOP and S5-TOP contain a larger amount of Pd_3Pb than samples S3-TOP and S3-BOT, in agreement with chemical analysis.

Considering the samples extracted from the same reactor (i.e., the S3 series), the overall concentration of Pb (as determined by chemical analysis) and the relative fraction of Pd_3Pb (as determined by XRPD) are both higher in the S3-TOP than in the S3-BOT sample. Taking into account that the CTA solution crosses the catalytic bed from top to bottom, the trend reflects the strong interaction between Pb and Pd [31] that takes place under the reactor's operating conditions, causing the preferential trapping of Pb in the uppermost catalytic layers.

Finally, for all the Pb-poisoned samples, the crystal size of Pd particles lies in the general sintering curve reported in the main part of Fig. 3. In addition, the crystal sizes of unpoisoned Pd and Pd_3Pb on the same sample are comparable (triangles in the inset of Fig. 3). This means that crystal sintering is unaffected by Pb contamination.

3.4. Co-contamination by S and Pb (S6 series)

In some cases, both Pb and S have been found on the same catalyst. This is the case for the S6 series, which has been withdrawn from different parts of the same reactor after only 1.5 months of industrial run. Pd particles in the three samples (i.e., S6-TOP, S6-MID, and S6-BOT) have a crystal size in agreement with what is expected for samples having had a short life (see the main part of Fig. 3), thus excluding the possibility that the loss of catalytic activity is due to rapid sintering of Pd crystals. As reported in Table 1,

the concentration of Pb as a function of the catalyst position in the reactor follows the same trend found for the samples of the S3 series, i.e., more concentrated at the top. The low S content does not allow us to evidence a clear trend.

The TEM image and the corresponding EDS maps shown in Fig. 7a–c confirm that both S and Pb are mainly located on Pd particles. Moreover, these maps demonstrate that they can be co-present on the same Pd agglomerate, even though a fraction of uncontaminated Pd is well evident. The map of Fig. 7d shows that the signals of Pb and S partly correlate, indicating that a specific Pd domain can be contaminated by only one contaminant or by both of them. An accurate statistical study performed on different regions of the catalyst reveals that, besides agglomerates partially contaminated with S and Pb, as shown in Fig. 7a–d, other Pd agglomerates contaminated either with S or with Pb are also present, as well as a relevant fraction of Pd agglomerates free from contaminants.

However, differently from the previously discussed cases, XRPD patterns (Fig. 7e) show the Pd reflections only, and other crystalline phases (such as the aforementioned Pd_4S and Pd_3Pb alloys or a Pb–S compound) are not present. Only a weak, unassigned peak at 38.7° makes an exception.

These data give an important warning on a possible limitation of XRPD, which, alone, is not sufficient to exclude the occurrence of chemical contamination, especially when the concentration of contaminants is low. In this case, both Pb and S may be present at the Pd surface as adatoms only, or even few monolayers of an alloy can be formed, but in both cases contamination of Pd particles would escape XRPD detection.

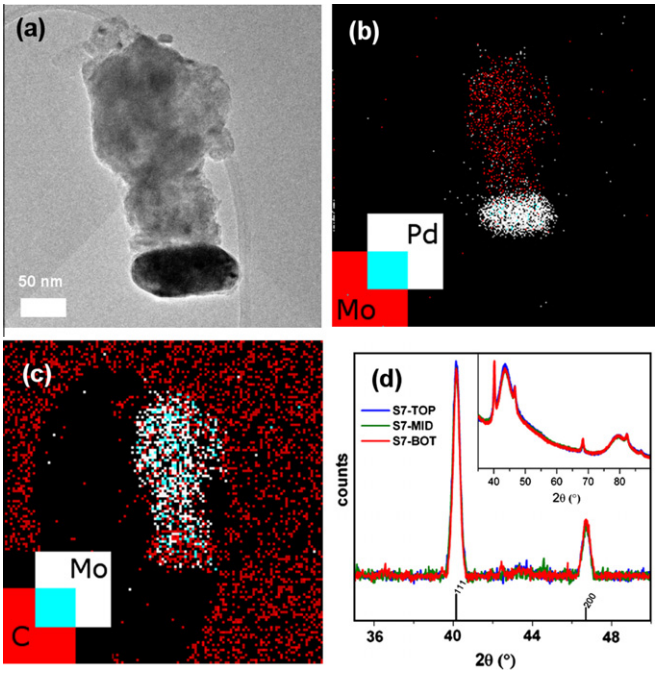

Fig. 8. Analysis of samples poisoned by Mo. (a) Selected TEM micrograph representing sample S7-TOP. (b–c) EDS maps of the same region shown in (a), showing the correlation between the fluorescence signals of Pd and Mo and Mo and C, respectively. (d) XRPD patterns of S7-TOP, S7-MID, and S7-BOT.

3.5. Contamination by Mo (S7 series)

Transition metals, such as Mo, Cr, Fe, and Ti, are common contaminants of Pd catalysts used in the purification of terephthalic acid. Due to the corrosive nature of mixtures of bromide ions and acetic acid, these metals are already originated in the stage preceding the purification unit, such as *p*-xylene oxidation [2] and the CTA drier [35]. Metal ions are potential poisons for metal catalysts [19,31,36]; in particular, in the purification of terephthalic acid, some transition metal ions can form insoluble terephthalates [34] deemed to be able to deactivate the catalyst [8].

Chemical analysis performed on samples belonging to the S7 series has revealed the presence of Mo as a contaminant in an amount that depends on the catalyst's position in the reactor, which is decreasing from top to bottom (Table 1). TEM and EDS analyses (Fig. 8a–c) have shown that Mo is distributed almost uniformly on the carbon support, independent of the presence of Pd metal particles. In Fig. 8b and c, a significant correlation between Mo and C fluorescence counts (part c) is observed, whereas the correlation between Mo and Pd counts (part b) is negligible. The absence of bulk Mo–Pd interaction is further supported by XRPD patterns (Fig. 8d), which show the reflections of Pd metal only. Moreover, the XRPD data provide evidence that no crystalline Mo phase has been formed, thus confirming the high dispersion of Mo atoms on the carbon support observed in the TEM investigation, even in S7-TOP sample where both the high Mo concentration and the high *Z* value of Mo should make any Mo-containing crystalline phase easily detectable by XRPD.

Besides the samples of S7 series, Mo is present in the overall set of samples investigated in this work (Table 1), although in different amounts. Specific EDS investigation has evidenced that in all cases the Mo fluorescence signal is correlated mainly with the C one, whereas no relationship with the Pd signal is observed. In a few cases, a very high local concentration of Mo counts has been observed, which, however, has never been detected as a crystalline phase in the electron diffraction patterns. We can therefore conclude that Mo contamination on the Pd catalyst is much less critical than S and Pb poisoning, because the Mo atoms adsorb mainly onto the support and not directly onto the active Pd phase. This is probably the reason why, although the Mo contamination level is relatively high, the catalyst of series S7 worked for 15 months inside the reactor.

3.6. Contamination by other elements (Cr, Fe, Ti and Al)

Other contaminants, such as Cr, Fe, Ti, and Al, are often co-present with the main contaminants discussed above (Table 1). The concentrations of such elements are significantly different from sample to sample. The origin of such metals and their main effects on Pd catalysts have been already discussed at the beginning of the previous section. In the whole set of samples investigated in our study, no evidence of crystalline phases involving Cr, Fe, Ti, and Al has been found in the XRPD patterns. Consequently, even in this case, the most informative technique to evidence a possible interaction between the contaminants and Pd has been EDS mapping. Fig. 9 reports a selection of TEM images and corresponding EDS maps that are representative of the distribution of Cr, Fe, Ti, and Al on the catalyst. No evidence of correlation between Pd and any of these contaminants has been found.

3.7. Effect of contamination on catalytic activity

The spent catalysts studied in this work have been unloaded from reactors because of low catalytic performance due to sintering or poisoning. As expected, the residual catalytic activity of all the catalysts (Table 1) is quite low, ranging between 5% and 16% of the activity of the stabilized catalyst, irrespective of the type and amount of contaminant. Unfortunately, it is not possible to define a direct relationship between the residual catalytic activity and any measurable catalyst property, because of the difficulty in

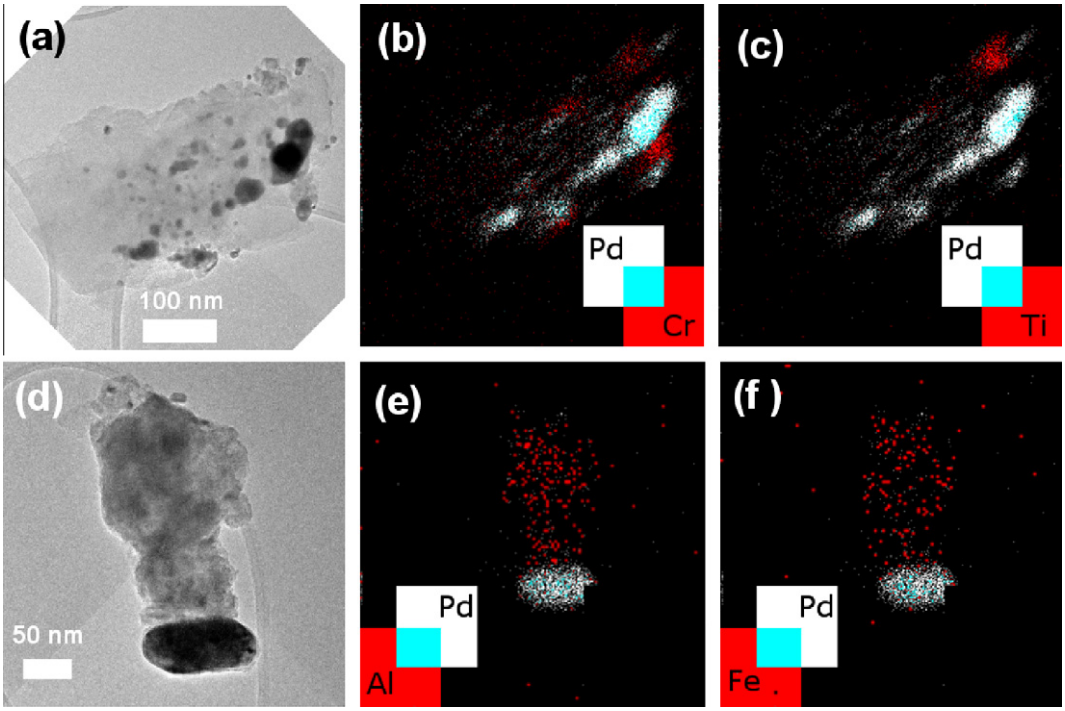

Fig. 9. TEM images representing sample S5-TOP (a) and S7-TOP (d), and corresponding EDS maps evidencing the relative location of Pd, Cr, Ti, Fe, and Al. The maps shown in (e and f) are reported with lower spatial resolution than the other maps reported so far because the small Fe and Al fluorescence counts forced us to merge adjacent pixels to reach sufficient statistics.

determining the fraction of "catalytically available" Pd surface. In fact, the residual Pd surface of a not poisoned, but sintered catalyst cannot be determined by the sintering degree of Pd crystals (measured by XRPD), because of the formation of aggregates (see Section 3.1). In addition, the surface contamination extent cannot be determined by XRPD, since we have demonstrated by EDS analysis that the absence of crystalline Pd_3Pb or Pd_4S phases is not sufficient to guarantee the absence of a poisoned surface (see Section 3.4). Unfortunately, even the more sensitive EDS analysis is not suitable to obtain a quantitative and statistically relevant measurement of uncontaminated Pd surface.

An alternative way to evaluate the data obtained from catalytic activity tests is to calculate the mean activity loss rate (i.e., activity loss per month of industrial run) as reported in Fig. 10. Sample S1 gives a value of 0.03, which can be considered as the reference, i.e., the loss rate in the presence of only "normal" sintering. A similar value is given by series S7, confirming that Mo and presumably Fe, Cr, Al, and Ti are neither poisonous nor sintering-inducing species, at least in the observed concentration range.

The rate of activity decay does not depend on the concentration of contaminant: Even surface poisoning is enough to deplete the catalytic activity. This is the case for catalysts belonging to the S6 series, which exhibit the most rapid activity loss, although the contaminant concentration is very low. These data provide evidence that (i) when present, S (and to a lesser extent Pb) has always a relevant and rapid negative effect on catalyst activity; and (ii) the stronger contamination of S2 samples by S did not occur linearly with time, but in the last period of catalyst life; otherwise the rate of activity loss would have been higher.

The activity loss rate of Pb-contaminated catalysts (S3–S5 series) is intermediate between that of unpoisoned and of S-poisoned catalysts. This would suggest that Pb has a lower poisoning power

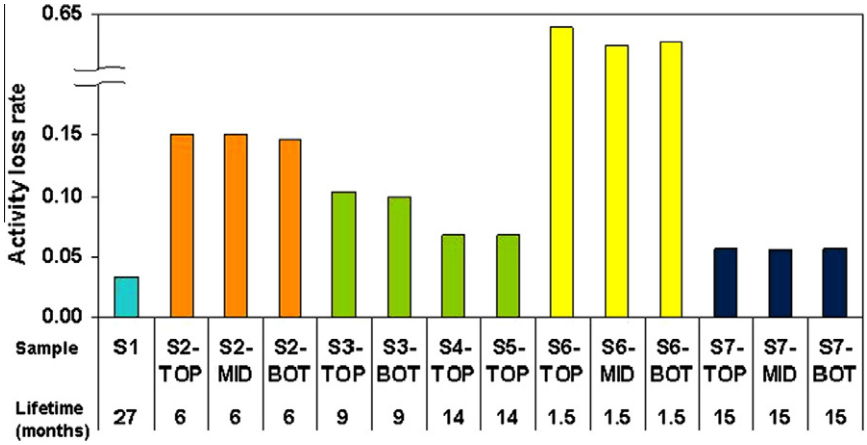

Fig. 10. Activity loss rate (i.e., activity loss per month of industrial run) of samples from Table 1.

than S. However, the observation that the catalysts with higher Pb content (S4–S5 series) show a smaller activity loss than those with lower Pb concentration (S3 series) suggests that also the contamination by Pb did not occur over the entire catalyst lifetime, but rather in a more limited period toward its end.

In light of these results, an activity loss rate higher than the "standard" one must be regarded as a sign of possible poisoning (not a measure of poisoning power or of contaminant concentration), which can be confirmed by XRPD or, if it fails, by EDS analysis.

4. Conclusions

With the aim of expand upon existing knowledge of the causes of deactivation of 0.5 wt.% Pd/C catalyst used for terephthalic acid hydropurification, a series of spent catalysts withdrawn from different industrial plants have been investigated.

Under normal operating conditions, the catalyst lifetime can exceed 2 years and the catalyst deactivation occurs because of Pd sintering, with loss of available Pd surface atoms. A precise image of this process has been obtained by the combined use of TEM, XRPD, and CO chemisorption, which, on the whole, have given information on the occurrence and evolution of isolated particles and aggregates and on their size. After initial fast stabilization of the smaller Pd particles with growth, the sintering continues slowly with the formation of Pd agglomerates where the Pd particles are welded together and, to a minor extent, of large isolated particles.

Besides slow Pd sintering occurring on a long time scale, poisoning phenomena may take place at any stage of the catalyst life, leading to rapid decay of catalytic performance, which obliges replacement of the catalyst before the expected time. Among all the investigated contaminants, S and Pb are the most dangerous, since they interact directly with the Pd, usually forming catalytically inactive Pd_4S and Pd_3Pb phases, easily detected by XRPD. However, even when the concentration of S or Pb on the catalyst is too low to give a bulk alloy and the poisoning is limited to the surface or subsurface Pd, the two contaminants are detrimental to catalytic performance; in these cases, EDS mapping is the best technique to reveal the presence of surface poisoning. Both S and Pb contaminants show a concentration profile along the catalytic bed, which has been elucidated.

Although often present in the spent catalysts, other metals such as Mo, Cr, Fe, Ti, and Al do not influence the catalyst performance significantly, since they interact mainly with the C support and not with the Pd active phase, as revealed by EDS mapping.

Acknowledgments

We are particularly grateful to Andrea Governini (Chimet SpA) for the catalytic activity measurements and to Massimo Graziani (Chimet SpA) for the chemisorption measurements. The authors thank Adriano Zecchina for the stimulating discussion. We are indebted with the whole staff of ESRF BM26 beamline (in particularly with S. Nikitenko) for the important and competent support during the Pd K-edge X-ray absorption experiments.

References

[1] R.J. Sheehan, Ullmann's Encyclopedia of Industrial Chemistry, Wiley-VCH Verlag, Weinheim, 1995.
[2] W. Partenheimer, Catal. Today 23 (1995) 69.
[3] P. Roffia, P. Calini, L. Motta, S. Tonti, Ind. Eng. Chem. Prod. Res. Dev. 23 (1984) 629.
[4] D.E. James, US Patent 4782,181, 1988.
[5] H. Köpnick, M. Schmidt, W. Brügging, J. Rüter, W. Kaminsky, Ullmann's Encyclopedia of Industrial Chemistry, Wiley-VCH Verlag, Weinheim, 1992.
[6] S.H. Jhung, A.V. Romanenko, K.H. Lee, Y.S. Park, E.M. Moroz, V.A. Likholobov, Appl. Catal. A Gen. 225 (2002) 131.
[7] http://www.hyosung.com/eng/product/chemical/tpa.jsp.
[8] N. Pernicone, M. Cerboni, G. Prelazzi, F. Pinna, G. Fagherazzi, Catal. Today 44 (1998) 129.
[9] J.B. Pelka, W. Paszkowicz, P. Dluzewski, M. Brust, C.J. Kiely, M. Knapp, E. Czerwosz, J. Alloys Compd. 328 (2001) 248.
[10] H.M. Rietveld, Acta Crystallogr. 22 (1967) 151.
[11] H.M. Rietveld, J. Appl. Crystallogr. 2 (1969) 65.
[12] A.A. Coelho, J. Appl. Crystallogr. 38 (2005) 455.
[13] S. Nikitenko, A.M. Beale, A.M.J. van der Eerden, S.D.M. Jacques, O. Leynaud, M.G. O'Brien, D. Detollenaere, R. Kaptein, B.M. Weckhuysen, W. Bras, J. Synchrotron Radiat. 15 (2008) 632.
[14] G. Silversmit, B. Vekemans, S. Nikitenko, W. Bras, V. Czhech, G. Zaray, I. Szaloki, L. Vincze, J. Synchrot. Radiat. 16 (2009) 237.
[15] C. Lamberti, S. Bordiga, F. Bonino, C. Prestipino, G. Berlier, L. Capello, F. D'Acapito, F.X. Llabres i Xamena, A. Zecchina, Phys. Chem. Chem. Phys. 5 (2003) 4502.
[16] B. Ravel, M. Newville, J. Synchrotron Radiat. 12 (2005) 537.
[17] S.I. Zabinsky, J.J. Rehr, A. Ankudinov, R.C. Albers, M.J. Eller, Phys. Rev. B 52 (1995) 2995.
[18] G. Agostini, R. Pellegrini, G. Leofanti, L. Bertinetti, S. Bertarione, E. Groppo, A. Zecchina, C. Lamberti, J. Phys. Chem. C 113 (2009) 10485.
[19] C.H. Bartholomew, Appl. Catal. A 212 (2001) 17.
[20] G. Agostini, E. Groppo, A. Piovano, R. Pellegrini, G. Leofanti, C. Lamberti, Langmuir 26 (2010) 11204.
[21] E.A. Owen, E.L. Yates, Philos. Mag. 16 (1933) 606.
[22] R. Pellegrini, G. Leofanti, G. Agostini, L. Bertinetti, S. Bertarione, E. Groppo, A. Zecchina, C. Lamberti, J. Catal. 267 (2009) 40.
[23] E. Groppo, W. Liu, O. Zavorotynska, G. Agostini, G. Spoto, S. Bordiga, C. Lamberti, A. Zecchina, Chem. Mater. 22 (2010) 2297.
[24] C.H. Bartolomew, P.K. Agrawal, J.R. Katzer, Advances in Catalysis, Academic Press, New York, London, 1982.
[25] A. Zubkov, T. Fujino, N. Sato, K. Yamada, J. Chem. Therm. 30 (1998) 571.
[26] F. Gronvold, E. Rost, Acta Crystallogr. 15 (1962) 11.
[27] C.H. Bartolomew, Appl. Catal. A Gen. 107 (1993) 1.
[28] E. Lamy-Pitara, Appl. Catal. 44 (1988) 261.
[29] T. Mallat, A. Baiker, Appl. Catal. A 200 (2000) 3.
[30] H.-U. Blaser, A. Indolese, A. Schnyder, H. Steiner, M. Studer, J. Mol. Catal. A Chem. 173 (2001) 3.
[31] T. Mallat, Z. Bodnar, S. Szabo, J. Petro, Appl. Catal. 69 (1991) 85.
[32] J.T. Szymanski, L.J. Cabri, J.H.G. Laflamme, Can. Miner. 35 (1997) 773.
[33] H. Schroeder, R.L. Wittman, US Patent 4808,751, 1989.
[34] F.G. Sherif, Ind. Eng. Chem. Prod. Res. Dev. 9 (1970) 408.
[35] Y. Gong, J. Cao, X.H. Meng, Z.G. Yang, Mater. Corros. 60 (2009) 899.
[36] T. Mallat, J. Petro, Appl. Catal. 57 (1990) 71.